EUROFUSION WPJET1-PR(16) 14916

KK Kirov et al.

Numerical calculations of non-inductive current driven by microwaves in tokamaks

Preprint of Paper to be submitted for publication in
Plasma Physics and Controlled Fusion

This work has been carried out within the framework of the EUROfusion Consortium and has received funding from the Euratom research and training programme 2014-2018 under grant agreement No 633053. The views and opinions expressed herein do not necessarily reflect those of the European Commission.

Numerical calculations of non-inductive current driven by microwaves in tokamaks

K. K. Kirov[1], Yu. Baranov[1], J. Mailloux[1], M. F. F. Nave[2] and JET Contributors[*]

EUROfusion Consortium, JET, Culham Science Centre, Abingdon, OX14 3DB, UK.
[1]CCFE Fusion Association, Culham Science Centre, Abingdon, United Kingdom
[2]Inst. de Plasmas e Fusão Nuclear, Inst. Superior Tecnico, Univ. de Lisboa, Lisbon, Portugal

Abstract: Recent studies at JET focus on analysis of the LH wave power absorption and CD calculations by means of a new Ray Tracing (RT) / Fokker-Planck (FP) package. The RT code works in real 2D geometry accounting for the plasma boundary and the launcher shape. LH waves with different parallel refractive index, $N_{\|}$, spectra in poloidal direction can be launched thus simulating authentic antenna spectrum with rows fed by different combinations of klystrons. Various FP solvers were tested including a new 3D relativistic bounce averaged FP code. LH wave power deposition profiles from the new code have been compared to the experimental results from electron cyclotron emission (ECE) analysis of pulses at 3.4T low and high density. This kind of direct comparison between power deposition profiles from experimental ECE data and numerical model are carried out for the first time for waves in the LH range of frequencies. The results are in a very good agreement with experimental data at lower density, line averaged values of $\bar{n}_e \approx 2.4 \times 10^{19}\ m^{-3}$. At higher density, $\bar{n}_e \approx 3 \times 10^{19}\ m^{-3}$, the code predicts more on-axis LH power deposition and very small absorption at the plasma periphery. The latter is inconsistent with the experimental observations and possible sources of these discrepancies have been briefly discussed in the paper. The code is also used to calculate the LH power deposition and CD profiles for the low-density preheat phase of JET's Advanced Tokamak (AT) scenario. It was found that as the density evolves from hollow to flat and then to a more peaked profile the LH power and driven current move inward i.e. towards the plasma axis. A total driven current of about 70kA for 1MW of launched LH power was predicted in these conditions.

Keywords: Ray Tracing and Fokker-Planck codes, LH waves absorption and CD, JET
PACS: 52.35.Hr, 52.40.Fd, 52.50.Sw, 52.55.Fa

* See the *Appendix of F. Romanelli et al., Proc. of the 25th IAEA Fusion Energy Conference, 2014, Saint Petersburg, Russia*

INTRODUCTION

Lower Hybrid (LH) waves are widely recognised as the most effective source of off-axis current in magnetically confined fusion experiments [1], [2], [3]. This fundamentally determines their main scope of use such as to drive a large amount of off-axis non-inductive current for fully non-inductive operation in advanced tokamak scenarios, for example the Steady State (SS) scenario, as well as for shaping the plasma current profile to avoid instabilities in the plasma core during the pre-heat and in the main heating phase. Based on these features LH system is also considered as one of the main microwave heating systems on ITER [4], [5] and a vital part in sustaining ITER SS scenario [6], [7]. Recent simulations [6] show that LH heating and Current Drive (CD) power of about 20MW can maintain SS scenario in ITER with minimum safety factor q of above 1.5, which is desirable with regard to avoiding neoclassical tearing modes.

LH waves' propagation, absorption and CD generation have been extensively studied numerically in the last three decades. A large number of numerical codes have been created, validated and subsequently tested and compared against each other, e.g. [3], [8]. It is acknowledged, however, that a more precise assessment of the LH power deposition and CD efficiency is required [9], [10], [11] for the purposes of possible ITER implementation.

Most of the present numerical tools, developed to deal with wave heating and CD problem in LH range of frequencies, fall into one of the following three categories: (*i*) Ray Tracing (RT) also called eikonal [12], [13] or Wenzel-Kramers-Brillouin (WKB) methods coupled with Fokker-Planck (FP) solver; (*ii*) Full Wave (FW) / Fokker-Plank codes and (*iii*) Particle-In-Cell (PIC) packages. The Ray Tracing / Fokker-Planck codes, which will be referred to as RT/FP codes, are the simplest in terms of physics background and computational power needs. These codes are the first to be used to study LH wave propagation and absorption. The so called geometric optics approximation used in this case, however, breaks down at the cut-offs at the plasma edge due to the sharp dielectric gradients there. In addition to this, in the pure RT case, the diffraction effects which occur at the caustics are not taken into account [13]. Recently paraxial treatment [14] of the eikonal and the so called beam tracing techniques were applied to solve this issue [15]. In the last decade more complex full wave solvers have been developed and successfully tested [16], [17]. Mixed WKB-full-wave approach has also been reported [18], [19]. Also in the recent years there is a significant progress in LH wave propagation modelling based on simulations with particle codes [20]. A summary of some of the advantages and disadvantages of the existing LH wave propagation codes is summarised in Table 1.

All the codes based on RT/FP and FW/FP models make use of the so called quasi-linear theory [21] to relate the wave electric field to the evolution of the Electron Distribution Function (EDF). The main difficulties here arise in the coupling between the wave propagation model and the Fokker-Planck solver. This is, in general, done by means of so called quasi-linear diffusion coefficient, D_{ql}, which relates the wave energy flux to diffusion in velocity space for the FP problem.

Table 1: Summary of the existing LH wave absorption and CD codes

	Advantages	**Disadvantages**
RT/BT	1. Simple and straightforward model implying simple computational model; 2. BT takes into account the geometry of the beam and diffractional effects at the caustics.	1. Not accurate in caustics and near cut-offs where the rays are reflected back to the plasma (geometrical optics breaks down); 2. RT does not take into account the geometry of the beam, so it does not account for the diffraction effects at the caustics.
FW	1. Comprehensive treatment of the wave behaviour near caustics and reflections from cut-offs.	1. Requires huge computational power; 2. The link between FW and FP is more complex which requires even more computational power.
PIC	1. Provides more complex picture of wave-particle interactions during wave propagation; 2. Non-linear Landau damping can treated.	1. Requires huge computational power; 2. Due to the large number of particles required only simple cases (e.g. cylindrical plasma, constant magnetic field and temperature) can be treated at the moment.

Presently a large amount of RT/FP codes, including those used at JET, are optimised for fast execution and aim at providing rudimentary estimates. The rays are usually traced in a simple 1D geometry. The same applies for the FP solvers which are hugely simplified due to requirements for quick processing. This paper presents details of a new more in-depth RT/FP code used at JET for LH wave propagation, absorption and CD calculations. The new suite of codes consists of separate RT and FP packages and is designed to account for all the issues mentioned above. It works with real plasma configuration of JET and deals with the realistic shape of the LH launcher. Various $N_{\parallel}$ spectra along poloidal length of the launcher can be used as well. In the following the basics of the RT and FP modules are discussed and some interesting results from the code at low and high plasma densities are presented. Comparison of the results from the code with the power deposition from experimental studies is a novel approach in analysing the LH wave absorption and details are highlighted in the paper. Section 2 discusses briefly the specifics of present day codes. Some details of the LHCD system and JET are provided as well. Structure of the new code is discussed in Section 4. Results of various tests and validation procedures are discussed in Section 5. The last part of the paper summarises the results and briefly discusses possible future applications of the code.

BRIEF OVERVIEW OF THE EXISTING RT/FP CODES

The existing RT / FP codes have two general parts: wave propagation module and Fokker-Planck solver.

There are various approximations which allow for simplification of the wave propagation problem. For instance, the application of ray equations and eikonal method can be used to provide an estimate of where in the plasma the microwave power is flowing. The so called geometric optics approximation used in this case, however, breaks down at the cut-offs at the plasma edge. This is even more pronounced in the case when the LH waves are weakly absorbed and propagation is in so called multi-pass absorption regime. In this case, the rays bounce between the plasma edges and caustics many times before being fully absorbed. As the number of bounces increases the stochasticity of the rays' position and wave vectors increases as well [22], [23], [47], [48]. In addition, in this approximation the diffraction effects which occur at the caustics are not taken into account [13]. Despite these minor disadvantages RT codes were widely used in all tokamaks with LH for treating wave propagation problem [7], [24], [25], [26], [27], [28], [29], [30], [31], [32], [33], [47], [49].

A number of FP codes with variable level of complexity can be found in the literature. The simplest solution is 1D non-relativistic treatment [1], [29], which employs 1D collision operator in a simplified form with contributions from collisional diffusion and drag coefficients, which are functions of the parallel velocity. Under this simplification the FP equation is reduced to an integral which can be solved numerically to provide the steady state electron distribution function (EDF). This approach is simple and does not allow for undesired negative values of EDF. Another more complex FP solver has been presented by Karney [34], [32]. It is fully relativistic and includes electric field treatment. Also, the collisions can be treated with the truncated collisional operator which is a more realistic approximation. As a result more consistent power deposition and CD profiles can be achieved. The most complicated FP solvers take into account the trapping effects as well, [35], [36], [37], [38], [39], [40].

In general, various combinations between wave propagation solvers and FP codes can be used. The only condition is that the wave absorption should be iterated consistently with FP by means of feeding the latter with D_{ql} from the wave equations, while in the iteration process the wave damping should be solved with EDF, f, from the FP code being used.

LHCD SYSTEM AT JET

The LH system at JET is capable of launching maximum about 6MW in L-mode plasmas at 3.7GHz. At high-density H-modes the available LH power is slightly lower due to coupling issues; in most of the experiments discussed here the coupled power was of the order of 2MW. The spectrum of the launched LH wave, expressed as a function of the RF power on the parallel refractive index $N_{||}$, can be changed by phase shifting the power delivered by each klystron. When the phases of the klystrons are selected so that there is no phase shift between adjacent multijunctions at the launcher mouth the spectrum can be presented as a narrow Gaussian curve peaked at $N_{||}$=1.83. Some of the experiments in SS scenarios at JET are performed at different launching spectrum, $N_{||}$=2.1 or $N_{||}$=2.3, achieved by a phase shift at the launcher of 45^{o} and 90^{o} respectively.

STRUCTURE OF THE NEW RT/FP CODE

The existing RT codes at JET, FRTC [24] and LHCD [25], are fast but this is achieved mainly by using a simplified geometry of the plasma and the launching structure. These

codes work well in cylindrical approximation assuming the LH wave is launched at the outer mid-plane and propagates in plasma with simple geometry. In reality the LH launcher has a finite poloidal geometry while the plasma is usually elongated and not up-down symmetric.

At JET a new RT/FP code (JRT) has been developed to address these issues and to study the impact of the real geometry of the LH launcher and the plasma shape and the real spectrum from various poloidal positions along the launcher. This way the code covers most realistic and interesting cases where the LH plant is pulsed with different klystrons' patterns in poloidal direction. Important problems, as for instance if launching different spectra from different rows affects the power deposition and CD efficiency, can be studied with the new model. In addition, the new code is also more portable and can be used with a number of FP solvers.

Some of the most essential features of the new RT/FP code include: (*i*) it works with the correct 2D geometry of the plasma; (*ii*) rays are launched according to the real geometry of the launcher; (*iii*) it has the capability to use different $N_{||}$ spectrum of the launched wave along different rows of the grill. These features are aiming at accurate simulation in real geometry emulating the real experimental conditions.

Ray tracing module.

The new code uses RT solver, which works in the real 2D plasma geometry. Rays are initially launched at the periphery of the plasma from locations corresponding to the LH launcher mouth. An iterative procedure then finds the exact location along the major radius at which density is equal to the cut-off density, $n_e = n_{e,\,SW\,cutoff}$. Rays start from that point assuming $N_\perp$=0 and then traced in the real *R*, *Z* geometry of the plasma.

The geometry used is right-handed cylindrical $\boldsymbol{R} = (R, \varphi, Z)$ with wave refractive index $\boldsymbol{N} = \boldsymbol{k}c/\omega = \boldsymbol{k}/k_0$ with components $(N_R, M=RN_\varphi, N_Z)$. The Ray Tracing equations then are:

$$\frac{dR}{dt} = -\frac{dD_0/dN_R}{\omega dD_0/d\omega};\ \frac{d\varphi}{dt} = -\frac{dD_0/dM}{\omega dD_0/d\omega};\ \frac{dZ}{dt} = -\frac{dD_0/dN_Z}{\omega dD_0/d\omega}; \qquad (1)$$

$$\frac{dN_R}{dt} = \frac{dD_0/dR}{\omega dD_0/d\omega};\ \frac{dM}{dt} = \frac{dD_0/d\varphi}{\omega dD_0/d\omega};\ \frac{dN_Z}{dt} = \frac{dD_0/dZ}{\omega dD_0/d\omega}$$

The spatial variables and *M* are normalized to 1m, the time to 1m/*c*, ω to 2π*1Hz and group velocity of the wave v_{gr}=(d*R*/d*t*; *R*dφ/d*t*; d*Z*/dt) to *c*.

The dispersion relation $D_0(\boldsymbol{R}, \boldsymbol{N}, t)$=0 used in (1) is expressed in terms of the perpendicular, $N_\perp = k_\perp / k_0$, and the parallel, $N_{||} = k_{||} / k_0$, refractive indexes:

$$D_0(\boldsymbol{R}, \boldsymbol{N}, t) = A_1\, N_\perp^6 + A\, N_\perp^4 + B\, N_\perp^2 + C = 0 \qquad (2)$$

$$\widehat{\boldsymbol{D}}_0 = \begin{pmatrix} S - N_{||}^2 & -iD & N_{||}N_\perp \\ iD & S - N_{||}^2 - N_\perp^2 & 0 \\ N_{||}N_\perp & 0 & P - N_\perp^2 \end{pmatrix}$$

with A_1, A, B, and C coefficients defined as

$$A_1 = -\left(\frac{3}{2}\frac{\omega_{pi}^2}{\omega^2}\frac{v_{ti}^2}{c^2} + \frac{3}{8}\frac{\omega_{pe}^2}{\Omega_{ce}^2}\frac{\omega^2}{\Omega_{ce}^2}\frac{v_{te}^2}{c^2}\right);$$

$$A = S;\ \ B = (S+P)\left(N_{||}^2 - S\right) + D^2;\quad C = P[\left(N_{||}^2 - S\right)^2 - D^2] \qquad (3)$$

where we use standard Stix notations for *S*, *P* and *D* in (3), while $N_{||} = k_{||}c/\omega$ and $N_\perp = k_\perp c/\omega$ are the parallel and the perpendicular refractive index.

Equilibrium data are presented in poloidal cross-section, i.e. (R, Z) geometry, while plasma kinetic profiles are assumed functions of the normalized toroidal flux radius ρ. The latter is regarded as prerequisite for interfaces with transport codes.

The present code does not include calculation of the launched spectra from the antenna, instead spectra from the SWAN code [41] were used. It is assumed that near Gaussian $N_{||}$ spectra are launched from launcher poloidal locations corresponding to waveguide sections.

The impact on the geometrical effects and the pitch of the magnetic field lines in front of the launcher are shown in figure 1 a). The launched spectra (in red) peaked at $N_{||}$ =1.83 for all the six rows (Row 1 to Row 6 for top to bottom, figure 1b) are downshifted (see dashed black curves) with respect to $N_{||}$ as shown for all rows. The spectra changes in some cases is significant, e.g. in rows 5 and 6 the launched spectrum is peaked at $N_{||}$ =1.82-1.84, while when the wave enters the plasma $N_{||}$ down-shifts to 1.77-1.79. It is also clear that not all the rows are affected in the same way, e.g. rows 1 and 2 are less affected than rows 5 and 6. It is clear from figure 1 a) that due to poloidal inhomogeneity proper treatment of the wave propagation problem requires raytracing in 2D geometry. The correct spectra are thus used to calculate the relevant power absorption and CD.

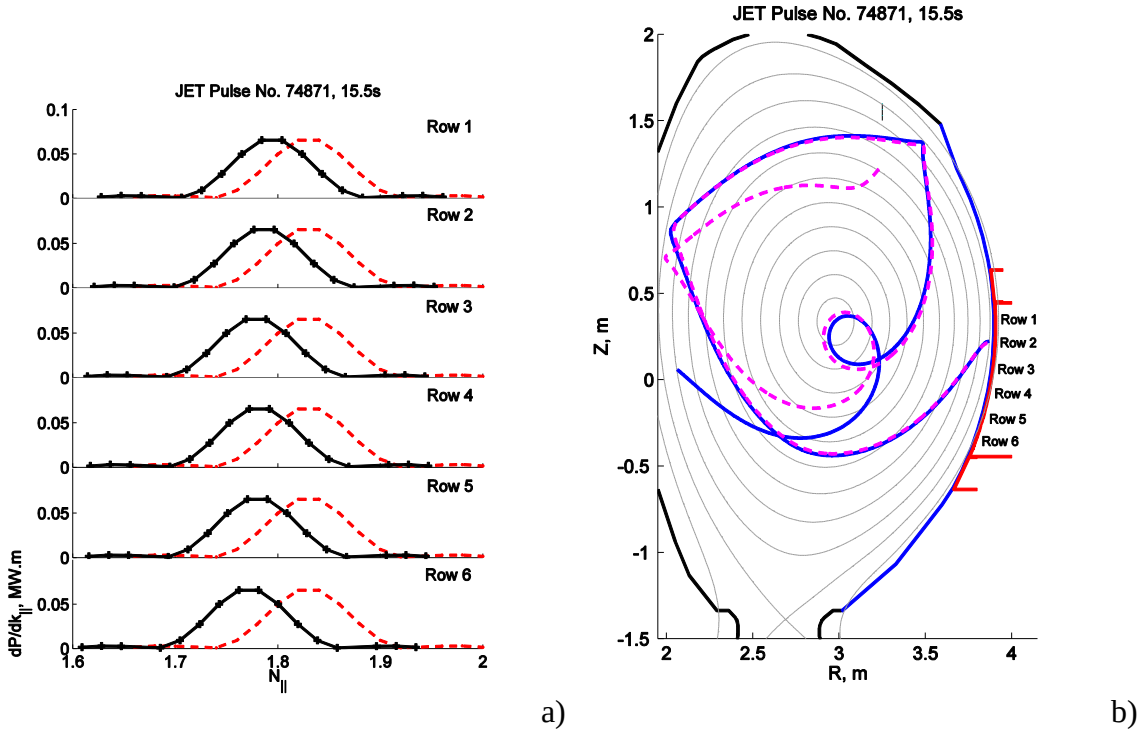

Figure 1: a) The launched (red dashed line) and the real (black solid line) spectra from rows 1 to 6. Power spectrum peaked at $N_{||}$ = 1.83, $dP/dk_{||}$ [MW.m] is plotted in the interval 1.6 < $N_{||}$ < 2 for $N_{||}$ box size of $\Delta N_{||}$ =0.02 and total launched power 0.5MW on rows 1 to 6 of the JET's LH launcher. b) JRT ray (blue line) launched from row 2 of LH launcher (profile in red on the right) is validated versus GENRAY result (dashed magenta line) for JET pulse #74871, 15.5s

The RT code is validated by comparing various ray paths with results from GENRAY code [30]. Different poloidal launching locations and different $N_{||}$ have been checked. In figure 1 b) an example with two traces of rays with $N_{||}$=1.8 launched at the mid-plane is

shown. The two rays in figure 1 b) are undistinguishable up to the point where they approach the caustic at the plasma centre. The deviation from this point on is due to the difference in the equilibrium meshes used in GENRAY and JRT.

LH wave absorption

Wave power absorption can be calculated by making use of the weak damping approximation, according to which the small imaginary part of the wave frequency, $\omega+i\gamma_t$, can be derived from the imaginary part of the dispersion relation (2) resulting from various damping mechanisms:

$$\frac{dP_r}{dt} = -2\,\gamma_t\,P_r\,; \quad \gamma_t \approx \frac{Im(D_0)}{\partial D_0/\partial\omega} \approx \frac{Im(P)\,\partial D_0/\partial P}{\partial D_0/\partial\omega} \tag{4}$$

Where P_r is the power in Watts carried by an individual ray, γ_t is the wave electric field damping rate. In the non-relativistic case of resonant damping on electrons:

$$Im(P) = -\pi\frac{\omega_{pe}^2}{\omega}\int_0^\infty 2\pi v_\perp dv_\perp \int_{-\infty}^\infty v_\parallel \frac{\partial f}{\partial v_\parallel}\delta(\omega - k_\parallel v_\parallel)dv_\parallel = \\ -\pi\frac{\omega_{pe}^2}{\omega}\int_{-\infty}^\infty v_\parallel \frac{\partial f_\parallel}{\partial v_\parallel}\delta(\omega - k_\parallel v_\parallel)dv_\parallel = -\pi\,\mathrm{sign}(k_\parallel)\frac{\omega_{pe}^2}{k_\parallel^2}\frac{\partial f_\parallel}{\partial v_\parallel}\Big|_{v_\parallel = v_{\parallel,res}} \tag{5}$$

where parallel EDF was introduced according to $f_\parallel(v_\parallel) = \int_0^\infty 2\pi v_\perp f dv_\perp$ and resonance parallel velocity $v_{\parallel,res} = \omega/k_\parallel$ is equal to the wave phase velocity.

In the relativistic case starting from the general expression for *P*, [32]:

$$P = \frac{\omega_{pe}^2}{\omega}\int_0^\infty 2\pi p_\perp dp_\perp \int_{-\infty}^\infty \frac{\partial f}{\partial p_\parallel}\frac{v_\parallel m_e}{(\omega - k_\parallel v_\parallel)}dp_\parallel \tag{6}$$

and after using the relation:

$$\frac{1}{\omega - k_\parallel v_\parallel} = P\left(\frac{1}{\omega - k_\parallel v_\parallel}\right) - i\pi\,\delta(\omega - k_\parallel v_\parallel) \tag{7}$$

one obtains for *Im*(*P*) at the resonance $\omega = k_\parallel v_\parallel$:

$$Im(P) = -\pi\frac{\omega_{pe}^2}{\omega}\int_0^\infty 2\pi p_\perp dp_\perp \int_{-\infty}^\infty v_\parallel m_e \frac{\partial f}{\partial p_\parallel}\delta(\omega - k_\parallel v_\parallel)dp_\parallel = \\ -\pi\frac{\omega_{pe}^2}{\omega}\int_{-\infty}^\infty v_\parallel m_e \frac{\partial f_\parallel}{\partial p_\parallel}\delta(\omega - k_\parallel v_\parallel)dp_\parallel \tag{8}$$

where parallel EDF was introduced according to $f_\parallel(p_\parallel) = \int_0^\infty 2\pi p_\perp f dp_\perp$.

By using the relations $v_\parallel m_e = p_\parallel/\gamma$, $\delta(\omega - k_\parallel v_\parallel) = \left(\gamma m_e/|k_\parallel|\right)\delta\left(p_{\parallel,res} - p_\parallel\right)$, where γ is the relativistic factor, $\gamma = \sqrt{1 + (p/m_e c)^2}$, and the resonance parallel momentum is defined as $p_{\parallel,res} = (\omega\gamma m_e/k_\parallel) = (c\gamma m_e/N_\parallel)$, after performing the integration over parallel momentum $p_\parallel$ one has for *Im*(*P*) the following expression:

$$Im(P) = -\pi\frac{\omega_{pe}^2}{\omega}\int_0^\infty 2\pi p_\perp dp_\perp \int_{-\infty}^\infty \frac{p_\parallel m_e}{|k_\parallel|}\frac{\partial f}{\partial p_\parallel}\delta\left(p_{\parallel,res} - p_\parallel\right)dp_\parallel = \\ -\pi\frac{\omega_{pe}^2}{\omega}\int_{-\infty}^\infty \frac{p_\parallel m_e}{|k_\parallel|}\frac{\partial f_\parallel}{\partial p_\parallel}\delta\left(p_{\parallel,res} - p_\parallel\right)dp_\parallel = -\pi\mathrm{sign}(k_\parallel)\frac{\omega_{pe}^2}{k_\parallel^2}\gamma m_e^2\frac{\partial f_\parallel}{\partial p_\parallel}\Big|_{p_\parallel = p_{\parallel,res}} = \\ -\pi\mathrm{sign}(k_\parallel)\frac{\omega_{pe}^2}{\omega^2}\frac{c}{N_\parallel^2}\gamma m_e^2\frac{\partial f_\parallel}{\partial p_\parallel}\Big|_{p_\parallel = p_{\parallel,res}} \tag{9}$$

Which transforms (4) into:

$$\frac{dP_r}{dt} = 2\pi\frac{\partial D_0/\partial P}{\partial D_0/\partial\omega}\mathrm{sign}(k_\parallel)\frac{\omega_{pe}^2}{\omega^2}\frac{c}{N_\parallel^2}\gamma m_e^2\frac{\partial f_\parallel}{\partial p_\parallel}\Big|_{p_\parallel = p_{\parallel,res}} P_r \tag{10}$$

FP solvers.

A number of FP solvers – from the simplest 1D model to more comprehensive codes as for instance CQL3D – can be used in conjunction with RT code. The present version of JRT has been tested with a number of different FP codes. A brief description of these is provided here.

The simplest approach is outlined by the 1D non-relativistic FP solver. The physics basis of it has been developed by Fish and Karney [1] and it is also used in [29]. Despite its simplistic form, this approach helps understanding the picture behind the wave heating and CD by LH waves in plasma. It can be also used when quick assessments of the CD are required, although, as it will be shown later it significantly overestimates the CD efficiency. It originates from the assumption that the parallel EDF, $F_{\|}$, and the collision operator, $\frac{\partial}{\partial v_{\|}}[(D_c(v_{\|})\,\partial/\partial v_{\|} + \nu_c(v_{\|})v_{\|})\,F_{\|}(v_{\|})]$, can be simplified as 1D functions on the parallel velocity, $v_{\|}$, only. Coefficients D_c and ν_c are calculated in high velocity limit and also depend on $v_{\|}$ and impurity content, Z_{eff}. This significant simplification of the problem allows for the 1D FP equation to be directly integrated, giving for the steady-state EDF the following integral expression:

$$F_{\|}(v_{\|}) = \frac{1}{\sqrt{2\pi v_t^2}} \exp\left(-\int_0^{v_{\|}} \frac{\nu_C(v'_{\|})v'_{\|}dv'_{\|}}{D_C(v'_{\|})+D_{ql}(v'_{\|})}\right) \quad (11)$$

The quasi-linear diffusion coefficient, D_{ql}, can be easily derived from the formula provided below. Although very simple this approach can still provide reasonable results and, in addition, it can work with large values of D_{ql}. Indeed, the denominator in the expression above allows for infinite values of the quasi-linear diffusion coefficient to be treated as well. It was found however that the 1D approach overestimates the driven current.

A more comprehensive approach is to use a 2D relativistic code as the one from Karney [34], which also includes electric field and relativistic effects. Similar approach is used in [32] as well. The transient relativistic full 2D equation which describes the evolution of the EDF f:

$$\frac{\partial f}{\partial \tau} = -\nabla_p \cdot \mathbf{S}\,, \quad \mathbf{S} = \mathbf{S_{ql}} + \mathbf{S_E} + \mathbf{S_c} \quad (12)$$

is solved numerically. The momentum $\boldsymbol{p}$ is presented in spherical co-ordinates (p, θ) where p is the absolute momentum and θ is the pitch angle, while the velocity v is $v = p/\gamma m_e$. The flux in momentum space can be presented as superposition of RF, $\mathbf{S_{ql}}$, electric field, $\mathbf{S_E}$ and collisional contributions, $\mathbf{S_c}$, whereby $\mathbf{S_{ql}}$ depends on the quasi linear diffusion coefficient. The absorbed RF power can be computed from the corresponding flux:

$$P_{\text{ql}} = \int \mathbf{v} \cdot \mathbf{S_{ql}} d^3\boldsymbol{p} \quad (13)$$

The 2D relativistic bounce-averaged solver is derived from an early version of Shoucri code [35], [36], [37] and apart from the normalisations it is similar to CQL3D [40]. A couple of modifications have been made to the code to account for the trapped particle profiles. An interface to the wave propagation code has been developed as well.

Assuming the bounce time $\tau_b = \oint' dl_b/|v_{\|}|$ is much smaller than the collisional time τ_{te} and ordering the FP equation in increasing order of $\tau_b/\tau_{te} \ll 1$ terms, one gets for the

first order EDF $f(p_0, \mu_0)$ computed on the Low Field Side (LFS) radial positions where magnetic field *B* is minimal:

$$\frac{\partial \lambda f}{\partial \tau} = -\nabla_p \cdot \lambda \mathbf{S} - \lambda I_0(f_{Max}, \mu_0 f_1) \quad (14)$$

where collisions were approximated by a contribution in divergence form, $\mathbf{S}_c^a$, accounted for in $\mathbf{S} = \mathbf{S_{ql}} + \mathbf{S}_E + \mathbf{S}_c^a$ and an integral contribution, $I_0(f_{Max}, \mu_0 f_1)$.

The '0' subscript in (p_0, μ_0) notation means these parameters are calculated at the LFS mid-plane minimum *B* points and are related to the local momentum and pitch angle by the relations:

$$p = p_0$$
$$\mu^2 = 1 - \psi(1 - \mu_0^2) \quad (15)$$

where $\psi = B_0/B$ is the ratio of the magnetic fields at LFS minimum and at the local point.

The parameter λ in (14) accounts for the bounce averaging and is related to the bouncing period τ_b:

$$\lambda = \left|v_{\|0}\right|\tau_b = |v\mu_0|\tau_b \approx 2qR_0(J_0 - 0.5\,\mu_T^2 J_2) \quad (16)$$

where the boundary between trapped and passing particles can be defined as $\mu_T = \sqrt{2\epsilon/(1+\epsilon)}$, with ϵ, q and R_0 being the device inverse aspect ratio, safety factor and major radius at the plasma axis. J_0 and J_2 are combinations of elliptic functions of the ratio μ_0/μ_T and can be found in [37].

The contributions to the flux in the momentum space, **S**, are flux surface and bounce averaged, meaning that the LH contribution from the quasi-linear diffusion coefficient has to be bounce-averaged as well.

Quasi-linear diffusion coefficient.

Mapping the wave energy carried by a particular ray into a quasi-linear diffusion coefficient, D_{ql}, is challenging. The procedure requires converting the power attributed to the ray into parallel wave electric field $\left|E_{\|}\right|^2$. Here some of the typical problems, related to the techniques being used in this paper, will be outlined. Comparison between different approaches will be discussed as well.

The general expression for D_{ql} has the following form:

$$D_{ql} = \frac{\pi}{2}\frac{e^2}{m_e^2}\left|E_{\|}\right|^2 \frac{k_{\|}^2 v_{\|}^2}{\omega^2}\delta(\omega - k_{\|}v_{\|}) \quad (17)$$

where $E_{\|}$ is the amplitude of the electric field parallel to the magnetic field. The delta function, δ, accounts for the resonant wave-particle interaction and in general there is no good numerical approximation for it.

An estimate of the parallel electric field can be found from the expression for the propagating wave energy density *U*:

$$\frac{P_r}{\boldsymbol{v_{gr}}\cdot\boldsymbol{S_\psi}} \approx \frac{P_r}{dV/dt} \approx \frac{P_r\,\Delta \mathrm{t}}{\Delta \mathrm{V}}\ ;\ \frac{P_r}{\boldsymbol{v_{gr}}\cdot\boldsymbol{S_\psi}} \approx U = \frac{\varepsilon_0}{4}\,\boldsymbol{E}^*\frac{\partial\omega\widehat{\boldsymbol{D}}_0}{\partial\omega}\boldsymbol{E} \quad (18)$$

where $\boldsymbol{v}_{\mathbf{gr}}$ is the wave group velocity, $\boldsymbol{S}_{\boldsymbol{\psi}}$ is the surface area of the flux surface being crossed by the ray, ΔV is the differential volume covered by ray element in Δt time interval. For slow wave in the electrostatic limit the following approximation can be used [42]:

$$\boldsymbol{E}^* \frac{\partial \omega \hat{\boldsymbol{D}}_0}{\partial \omega} \boldsymbol{E} \approx \omega \left(\frac{N_\perp^2}{N_\parallel^2} \frac{\partial S}{\partial \omega} + \frac{\partial P}{\partial \omega} \right) |E_\parallel|^2 \quad (19)$$

Replacing (19) in (18) and using (17) one gets the following contribution to the quasi-linear diffusion coefficient from a particular ray:

$$D_{ql} = \frac{\pi}{2} \frac{e^2}{m_e^2} \frac{4}{\varepsilon_0} \frac{1}{\omega \left(\frac{N_\perp^2}{N_{||}^2} \frac{\partial S}{\partial \omega} + \frac{\partial P}{\partial \omega} \right)} \frac{P_r \, \Delta \mathrm{t}}{\Delta \mathrm{V}} \delta(\omega - k_{||} v_{||}) =$$

$$\frac{\pi}{2} \frac{e^2}{m_e^2} \frac{4}{\varepsilon_0} \frac{1}{\frac{N_\perp^2}{N_{||}^2} \frac{\partial}{\partial \omega} \left(\omega \frac{D_0}{N_\perp^4} \right)} \frac{P_r \, \Delta \mathrm{t}}{\Delta \mathrm{V}} \delta(\omega - k_{||} v_{||}) \quad (20)$$

The denominator in the last equation (20) is further simplified by the approximation $\omega \left(\frac{N_\perp^2}{N_{||}^2} \frac{\partial S}{\partial \omega} + \frac{\partial P}{\partial \omega} \right) \approx \frac{N_\perp^2}{N_{||}^2} \frac{\partial}{\partial \omega} \left(\omega \frac{D_0}{N_\perp^4} \right)$ which has been used by Bonoli [28] and in 1D case [29].

Alternatively, one can derive the quasi-linear diffusion coefficient, D_{ql}, by comparing the expression for the wave power damping equation with the absorbed RF power as calculated from FP. This approach is used in the 2D relativistic case by Imbeaux and Peysson [32]. Starting from the expression for wave power absorption, eqs. (4) and (10), we have for the ray's power damped in a time interval of Δt the following expression $\Delta P_r = -2\gamma_t P_r \Delta t$, while for the absorbed power in the momentum interval $p_{||}$, $p_{||} + dp_{||}$ from (10) one can use the following approximation:

$$dP_r|_{p_\parallel}^{p_\parallel + dp_\parallel} = 2\,\pi \, \frac{\partial D_0/\partial P}{\partial D_0/\partial \omega} \frac{\omega_{pe}^2}{\omega} \frac{p_\parallel m_e}{|k_\parallel|} \frac{\partial f_\parallel}{\partial p_\parallel} \delta(p_{\parallel,res} - p_\parallel) dp_\parallel P \Delta t =$$

$$2\,\pi \, \frac{\partial D_0/\partial P}{\partial D_0/\partial \omega} \frac{\omega_{pe}^2}{\omega} \frac{p_{\parallel,res} m_e}{|k_\parallel|} \frac{\partial f}{\partial p_\parallel}\Big|_{p_\parallel = p_{\parallel,res}} \delta(p_{\parallel,res} - p_\parallel) dp_\parallel P \Delta t \quad (21)$$

In addition, the absorbed power can be calculated from the FP code providing D_{ql} is known:

$$P_{ql} = -n_e \Delta \mathrm{V} \int_0^\infty 2\pi p_\perp dp_\perp \int_{-\infty}^\infty dp_\parallel \, D_{ql} \frac{p_{\parallel,res}}{\gamma m_e} \frac{\partial f}{\partial p_\parallel}\Big|_{p_\parallel = p_{\parallel,res}} =$$

$$-n_e \Delta \mathrm{V} \int_{-\infty}^\infty dp_\parallel \, D_{ql} \frac{p_{\parallel,res}}{\gamma m_e} \frac{\partial f_\parallel}{\partial p_\parallel}\Big|_{p_\parallel = p_{\parallel,res}} \quad (22)$$

Expression (22) can be also transformed into the following expression for the absorbed power in the momentum interval $p_{||}$, $p_{||} + dp_{||}$ [32]:

$$dP_{ql}|_{p_\parallel}^{p_\parallel + dp_\parallel} = n_e \Delta \mathrm{V} D_{ql} \frac{p_{\parallel,res}}{\gamma m_e} \frac{\partial f_\parallel}{\partial p_\parallel}\Big|_{p_\parallel = p_{\parallel,res}} dp_\parallel \quad (23)$$

The quasi-linear diffusion coefficient can then be found after equalling $dP_r|_{p_\parallel}^{p_\parallel + dp_\parallel}$ from expressions (21) and $dP_{ql}|_{p_\parallel}^{p_\parallel + dp_\parallel}$ from (23) resulting in the following expression for D_{ql}:

$$D_{ql}(p_\parallel) = \frac{2\pi}{n_e} \frac{\partial D_0/\partial P}{\omega \partial D_0/\partial \omega} \frac{\omega_{pe}^2}{\omega} P_r \frac{\Delta t}{\Delta \mathrm{V}} \frac{\gamma m_e^2}{|k_\parallel|} \delta(p_{\parallel,res} - p_\parallel) =$$

$$\frac{\pi}{2} e^2 \frac{4}{\varepsilon_0} \frac{N^2 N_\parallel^2}{\omega \partial D_0/\partial \omega} P_r \frac{\Delta t}{\Delta \mathrm{V}} \frac{\gamma m_e}{\omega |k_\parallel|} \delta(p_{\parallel,res} - p_\parallel) \quad (24)$$

A close look to (24) reveals that in typical LH wave propagation regime $N^2 = N_\perp^2 + N_\parallel^2 \approx N_\perp^2$ it is in general the relativistic form of (20).

More comprehensive 2D bounce averaged relativistic codes as those from Shoucri [35] and CQL3D [40], also treat the trapping effects. In this case EDF is a function of the momentum p and pitch angle θ with $\mu = \cos\theta$. The corresponding quasi-linear diffusion

coefficient now accounts for the trapping effects and we derive it directly from the expression for δB_0 from the CQL3D manual [40]:

$$D_{ql}(p_0,\mu_0) = \frac{\delta s_{pol}}{2\pi\Delta\Psi}\frac{\mu_0}{\mu}|B|\frac{\delta\tilde{B}}{\tilde{S}_{pol}}\frac{\Delta P}{\Delta k_\parallel} = \frac{\pi}{2}e^2\frac{4}{\varepsilon_0}\frac{\partial D_0/\partial P}{\omega\partial D_0/\partial\omega}\frac{\delta s_{pol}}{v_{grpol}}\left[\frac{1}{2}\frac{1}{4\pi R_0}\frac{1}{\Delta l_\Psi}\frac{1}{qR}\frac{|B|}{B_p}\frac{1}{(J_0-0.5\,\mu_T^2 J_2)}\frac{\mu_0}{\mu}\right]P_r\delta(\omega-k_\parallel v_\parallel) \quad (25)$$

In CQL3D notations $\tilde{S}_{pol} \approx v_{grpol}\frac{\varepsilon_0}{4}\boldsymbol{E}^*\frac{\partial\omega\widehat{\boldsymbol{D_0}}}{\partial\omega}\boldsymbol{E}\frac{1}{|E_\parallel|^2} \approx v_{grpol}\frac{\varepsilon_0}{4}\frac{\partial\omega S}{\partial\omega}\Delta k_\parallel$ is the normalised wave energy flux, $v_{\rm grpol}$ is the poloidal projection of the wave group velocity, $\delta s_{\rm pol}$ is the poloidal projection of the ray element, $\Delta l_\Psi = \Delta\Psi/|\nabla\Psi|$ is the width perpendicular to the flux surface of a volume element containing the ray element and Ψ is the poloidal flux function. The variable $\mu = \cos\theta = \sqrt{1-\psi\sin^2\theta}$ is calculated according to (15) for values of ψ taken at the local coordinate. The rest of the variables have the usual meanings: R is the plasma major radius at the point of interest, B and B_p are the total and the poloidal magnetic field also calculated at the point of interest. The expression for the non-trapping case can be quickly recollected noting that $\Delta t = \delta s_{pol}/v_{gpol}$ and $\Delta l_\Psi = \Delta\Psi/|\nabla\Psi|$, $|\nabla\Psi| = RB_p$, $q \approx rB_T/R_0B_p$ and in large aspect ratio approximation $\mu_T \to 0$, $J_0 \approx \pi/2$ and $\mu_0/\mu \approx 1$ and resulting in $\left[\frac{1}{2}\frac{1}{4\pi R_0}\frac{1}{\Delta l_\Psi}\frac{1}{qR}\frac{|B|}{B_p}\frac{1}{J}\frac{\mu_0}{\mu}\right] \approx 1/(4\pi^2 rR_0\Delta l_\Psi) \approx 1/\Delta V$.

Numerical implementation.

The velocity in the 1D FP solver is normalised to the thermal one, $v_t = \sqrt{T_e/m_e}$, while in the relativistic case the momentum p is normalised to the thermal momentum $p_t = m_e v_t$. In the latter case $v_{\rm t}$ is different from the thermal velocity, which we define as $V_{te} = v_{te}\sqrt{1-5\Theta/2+55\Theta^2/8-\cdots}$ with Θ parameter equal to $\Theta = T_e/m_ec^2 = v_t^2/c^2$. The electron temperature used in these normalisations, T_e, can be either the local electron temperature or in bounce-averaged case a fixed value of $T_{\rm e}$ is selected for all EDFs along the plasma profile. In normalised units, $\tilde{p} = p/p_t = p/m_ev_t = p/\sqrt{m_eT_e}$, while the EDF $\tilde{f} = (mT_e)^{3/2}f$ so that $\int\tilde{f}d^3\tilde{p} = 1$.

In solving the FP equation the time is normalised to the collisional time, $\tau = t/\tau_{te} = t\nu_t$, with $\tau_{te} = 4\pi\varepsilon_0^2m_e^2v_t^3/n_eq_e^4ln\Lambda$ where $ln\Lambda$ is the Coulomb logarithm. The power density is normalised to $n_ep_t^2/m_e\tau_t$, quasilinear diffusion coefficient to p_t^2/τ_t, the electric field to $p_t/q_e\tau_{te}$ and the current density to $n_eq_ep_t/m_e$. Expression (10) for the LH power absorption in normalised units converts into:

$$\frac{dP_r}{dt} = 2\pi\frac{\partial D_0/\partial P}{\partial D_0/\partial\omega}\text{sign}(k_\parallel)\frac{\omega_{pe}^2}{\omega^2}\frac{\gamma}{N_\parallel^2}\frac{1}{\Theta_1}\frac{\partial\tilde{f}_\parallel}{\partial\tilde{p}_\parallel}\Big|_{\tilde{p}_\parallel=\tilde{p}_{\parallel,res}}P_r \quad (26)$$

where the normalised resonance parallel momentum $\tilde{p}_{\parallel,res}$ is defined as $\tilde{p}_{\parallel,res} = \frac{\gamma}{N_{||}}\frac{1}{\sqrt{\Theta}}$.

The quasilinear diffusion coefficient, $D_{\rm ql}$, in the equations (20) to (25) involves δ function calculations. Depending on whether relativistic or non-relativistic FP code is used the Dirac delta function can be approximated in different ways. In the non-relativistic case where $\tilde{v} = v/v_{te}$ we have:

$$\delta(\omega-k_\parallel v_\parallel) = \frac{1}{|k_\parallel|v_{te}}\delta\left(\tilde{v}_{\parallel,res}-\tilde{v}_\parallel\right) = \frac{1}{\omega}\frac{1}{|N_\parallel|\sqrt{\Theta}}\delta\left(\tilde{v}_{\parallel,res}-\tilde{v}_\parallel\right) \quad (27)$$

with $\tilde{v}_{\parallel,res} = 1/(N_\parallel\sqrt{\Theta})$. In the relativistic case the replacement $v_\parallel = p_\parallel/\gamma m_e$ needs to be made and with the normalisation $\tilde{p} = p/p_{te}$ the above expression for transforms into:

$$\delta(\omega - k_\parallel v_\parallel) = \frac{1}{\omega}\frac{\gamma}{|N_\parallel|\sqrt{\Theta}}\delta\left(\tilde{p}_{\parallel,res} - \tilde{p}_\parallel\right) \quad (28)$$

where $\tilde{p}_{\parallel,res} = \gamma/\left(N_\parallel\sqrt{\Theta}\right)$.

In the bounce-averaged case the momentum is normalized to the thermal momentum, p_{t1}, defined for a fixed temperature, e.g. 1keV, $\tilde{p}_1 = p/p_{t1}$. The values of $\tilde{p}_{1,0}$ and μ_0 are taken at the outer mid-plane at the minimum of the B field. Delta function can be rewritten for $\tilde{p}_{1,||} = \tilde{p}_{1,0}\mu_0$ variable with $\delta(\omega - k_{||}v_{||}) = \frac{1}{\omega}\frac{\gamma}{|N_{||}|\sqrt{\Theta_1}}\delta\left(\tilde{p}_{1||} - \tilde{p}_{1||,res}\right)$, with $\tilde{p}_{1,||res} = \gamma/\left(\left|N_{||}\right|\sqrt{\Theta_1}\right)$, where Θ_1 is calculated at fixed temperature, e.g. 1keV. A common problem in interfacing RT code and FP solver is the numerical implementation of the Dirac delta function in momentum space. A too narrow function can lead to comb-like EDF plateau while too broad approximation will overestimate the absorbed LH power. There are various ways to represent numerically the Dirac δ function. For instance, one can use a boxcar or step function. Other possibility, which is mainly used here, is to use a Gaussian approximation:

$$\delta(1-x) \approx \frac{1}{\Delta\sqrt{\pi}}e^{-(1-x)^2/\Delta^2} \quad (29)$$

Another issue in the numerical calculations, which is a possible source of errors, is in converting the quasilinear diffusion coefficient, D_{ql}, from wave propagation equation to the one for FP code. Usually D_{ql} from wave propagation is calculated in ($p_\parallel$, $p_\perp$) coordinates while FP codes use (p, μ=cos(θ)) coordinates hence a mapping into the new coordinates is needed.

At relatively high power the normalized D_{ql} from wave propagation is quite large and results in numerical instabilities in the FP solver, so it often needs reducing. It was found [32] that the FP codes work well by limiting the normalised D_{ql} to 10, which is adopted in our model. A good estimate of the RT/FP convergence is by comparing the absorbed power density, p_{LH}, from the wave equation (10) (or alternatively (21)) mapped into the flux surface to derive the power deposition profile, p_w, and the one calculated by the FP code, p_{ql}, as in (13) (or alternatively (22)). The values of the total power, derived after integration over the plasma volume, P_w, and, P_{ql}, in all of the calculations presented here differ by maximum of about 30%. In the paper absorbed power, P_w, is provided when discussing the power deposition profiles, while the CD profiles are estimated from the CD efficiency from the FP code, which is multiplied to P_w to get the corresponding CD profile.

POWER DEPOSITION AND CURRENT DRIVE CALCULATIONS

RT/FP calculations require iterative procedure between wave absorption calculations and the FP solver in order to derive consistent power deposition profiles. Ideally, after first few iterations the absorbed power from the FP code converges towards the one calculated by the wave absorption module. Errors in the two modules usually result in discrepancies in absorbed power and this can be used as a tool to debug the codes used in the numerical calculations. In the following, the power deposition profiles derived from the wave absorption eq.(10) and from the FP solver eq.(13) are compared between each other and

then to the power deposition profiles derived in early experimental studies on the EC emission.

Comparison between different FP solvers

The power deposition profiles from 1D and 2D relativistic FP solvers are calculated and compared to the experimental findings in two JET pulses: (*i*) low density 3.4T/1.5MA JET pulse #77609 and; (*ii*) high density 3.4T/1.8MA JET pulse #77609. In the first case density line averaged values were about $\bar{n}_e \approx 2.4 \times 10^{19}\, m^{-3}$, while the central electron temperature was of the order of $T_{e0} \approx 3keV$, i.e. a relatively cold plasma in L-mode with small amount (<1.4MW) NBI power for diagnostic purposes. In the second case line averaged density was of the order of $\bar{n}_e \approx 3 \times 10^{19}\, m^{-3}$ with H-mode like density pedestal and higher central electron temperature $T_{e0} \approx 3.5keV$ was achieved by applying ~9.5MW of NBI power. Density and temperature profiles in these two pulses are shown in figure 2 and were kept constant during the LH heating phase. The LHCD power peaked at $N_{||}$=1.83 was modulated in the first 3 seconds and then cw power with the same averaged values - 1.9MW (#77609) and 1.8MW (#77612) - was applied. The power deposition profiles during the modulated phase was studied and experimentally estimated in [43] and the conclusions were backed up by analysis of the non-thermal ECE emission [44].

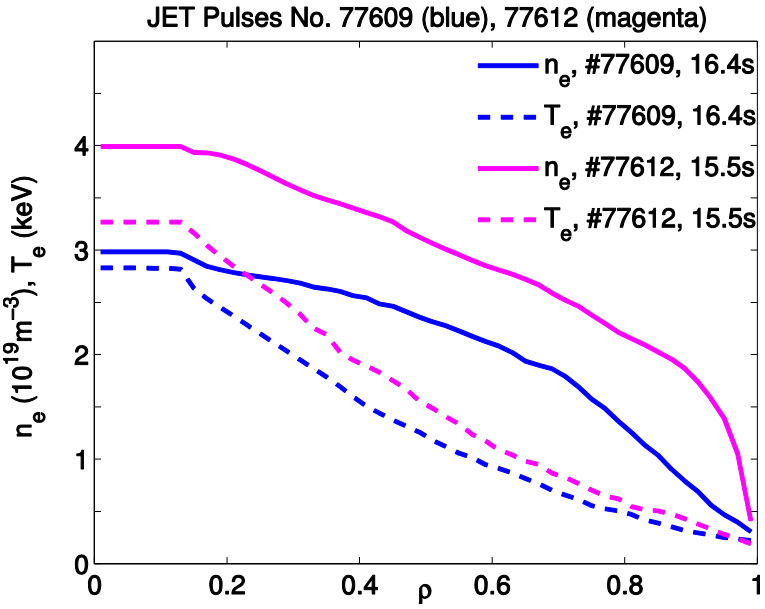

Figure 2: Plasma density (blue) and temperature (magenta) profiles for the low density 3.4T/1.5MA JET pulse #77609 (solid lines) and high density 3.4T/1.8MA JET pulse #77612 (dashed lines).

Power deposition profiles from 1D and 2D relativistic and 2D relativistic bounce-averaged codes are shown in figure 3. In the latter case two cases with temperature normalisations of T_{e0}=1keV and T_{e0}=2keV were considered.

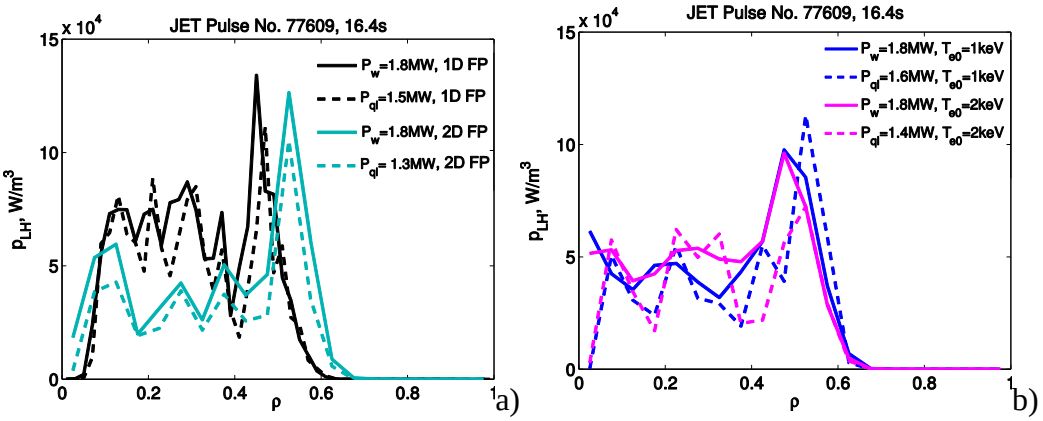

Figure 3: Comparison of power deposition profiles from wave damping (p_w, solid lines) and from FP solver (p_{ql}, dashed lines) as derived from 1D (black lines) and 2D (cyan lines) relativistic codes a) and 2D relativistic bounce-averaged code b) for low density JET 3.4T/1.5MA pulse #77609. In b) two profiles are shown: one for temperature normalisation of T_{e0}=1keV (blue lines) and one for T_{e0}=2keV (magenta lines). The amount of the total absorbed power from the wave absorption calculations, P_w, and the FP results, P_{ql}, are provided in the legends.

In all four cases in figure 3a and 3b power deposition profiles from wave absorption, p_w, and from FP code, p_{ql}, are consistent and converge reasonably well within the first 6-7 iterations. The total amount of absorbed power from the wave damping, P_w, agrees well with FP solver value, P_{ql}, as shown in the legends. In the 1D and 2D relativistic case, figure 3a, it was found that these two values are very close with FP results being about ~10% lower. Discrepancy is larger in the 2D bounce-averaged case with T_{e0}=2keV, figure 3b, where the absorbed power calculated by FP code was about 25% lower. It was found, however, that after reducing the spatial mesh size, e.g. by increasing the number of points of ρ from 21 to 51 points, this discrepancy can be reduced to about ~10%. Comparing the four cases, one concludes that all 2D relativistic cases are consistent and show a broad power deposition profile with density of about 5×10^4 W/m^2 between magnetic axis and normalised toroidal radius of ρ=0.6. The 1D case is slightly narrower with power density of about 7×10^4 W/m^2 in the region $0.1<\rho<0.5$.

In figure 4a and 4b the power deposition profiles from 1D and 2D relativistic FP solvers and 2D relativistic bounce-averaged code with two temperature normalisations, T_{e0}=1keV and T_{e0}=2keV, are shown for higher density JET pulse #77612.

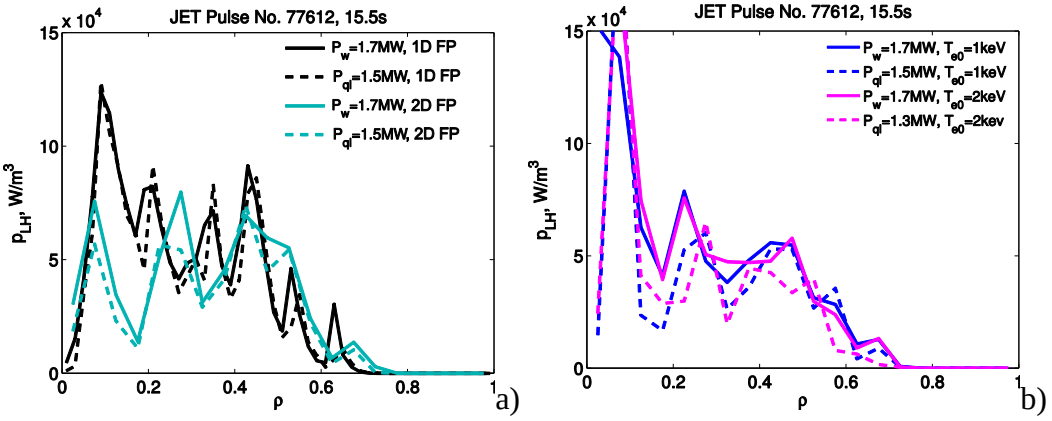

Figure 4: Comparison of power deposition profiles from wave damping (p_w, solid lines) and from FP solver

(p_{ql}, dashed lines) as derived from 1D (black lines) and 2D (cyan lines) relativistic codes a) and 2D relativistic bounce-averaged code b) for high density JET 3.4T/1.8MA pulse #77612. In b) two profiles are shown: one for temperature normalisation of T_{e0}=1keV (blue lines) and one for T_{e0}=2keV(magenta lines). The amount of the total absorbed power from the wave absorption calculations, P_w, and the FP results, P_{ql}, are provided in the legends.

Here again the power deposition profiles for the 1D and 2D relativistic FP cases are consistent, while the coarse spatial mesh in the second case results FP power deposition being about 25% lower than the one calculated by wave absorption. Here again choosing finer mesh seems to cure the problem and FP power is within 15% of the one from the wave absorption. Comparing the latter from the four cases – 1D, 2D relativistic and 2D relativistic bounce-averaged with T_{e0}=1keV and T_{e0}=2keV – one finds that there is a small discrepancy in the central absorption. In the 1D and 2D relativistic cases, figure 4a, no power is absorbed on-axis, while in the 2D relativistic bounce-averaged case, figure 4b, some power is absorbed in the very core. For ρ>0.2 all four cases are consistent with power densities of about 5×10^4 W/m^2.

The CD profiles for the two pulses discussed above are shown in figure 5. They are calculated by deducing the CD efficiency from the FP solver and then multiplying it to the power density from the wave absorption. In the low density case, figure 5a, the two 2D FP codes are in a reasonably good agreement regarding the current drive profile, j_{LH}, and total CD, I_{LH}. The latter is of the order of 0.15MA by the 2D relativistic and 0.14MA by the bounce averaged FP codes. In the 1D case twice larger CD is predicted with I_{CD} =0.28MA. This large overestimate of the CD by the 1D approach means it is not applicable in our case.

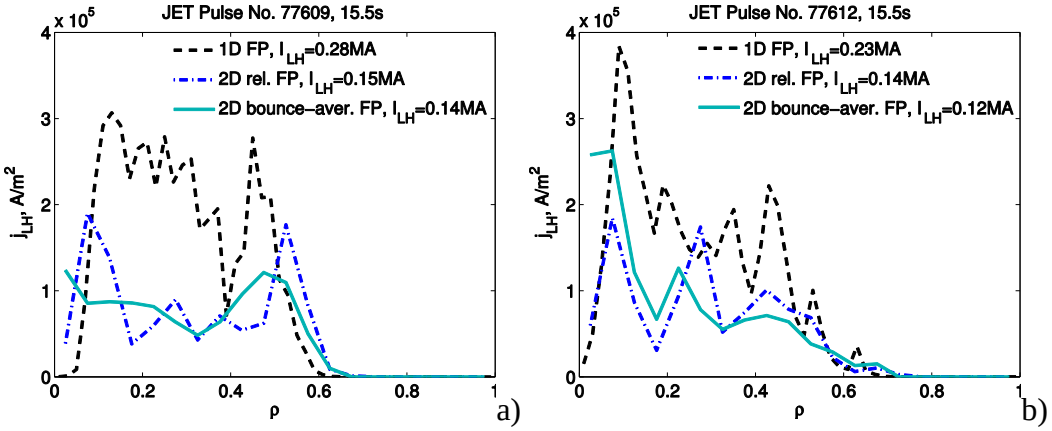

Figure 5: Current drive profiles from 1D (black dashed lines), 2D relativistic (blue dash-dotted lines) and 2D relativistic bounce-averaged FP with T_{e0}=1keV (solid cyan lines) codes for low density JET pulse #77609 a) and high density JET pulse #77612 b). The total amount of the driven current for each case is provided in the legends.

In the high density case, figure 5b, the two 2D FP codes differ slightly with respect to the current drive profile, j_{LH}, but are more consistent regarding the total driven current, I_{LH}. The latter is again slightly lower, 0.12MA, in the bounce averaged FP case compared to 2D relativistic case, where total driven current of 0.14MA is predicted. As in the previous case, the 1D approach overestimates by factor of about 2 both the driven current density j_{LH} and the total CD, I_{CD} =0.23MA.

Validation of the FP solver

The RT code and the relativistic FP solver were verified against experimentally validated LH deposition profiles. The LH wave power depositions for the two pulses, #77609 and #77612, were studied experimentally at JET by applying modulated LH power [43] as well as analysing the emission of the supra-thermal electrons [44]. In both cases it was concluded that the deposition is off-axis and very broad. These experimentally verified power deposition profiles are now compared to the results from JRT.

In figure 6 results of the LH power deposition profiles from JRT (solid line) and experimentally verified ones for JET pulse #77609 are shown. The experimental profiles were determined from modulation experiments (dash-dotted line) and alternatively from the EC emission of the supra-thermal electrons (dashed line). The JRT code also predicts broad off-axis deposition in this case. Although the code predicts more ragged profile, the calculations are in a very good agreement with experimental data. This kind of direct comparison between calculated and experimentally assessed power deposition from the ECE measurements is reported for the first time in the literature on the LH waves. One area of improvement is the missing deposition at the periphery as the code predicts no LH power for $\rho>0.63$, while there is experimental evidence that LH power is absorbed for up to $\rho=0.8$-0.9. The code also overestimates the absorbed power at $\rho\sim0.5$. Despite these discrepancies the total absorbed power, P_{LH}, from JRT is 1.8MW and is in an excellent agreement with the actual value of about 1.9MW. The total driven current in this case has been assessed of the order of $I_{LH} \approx 0.14MA$, figure 5a.

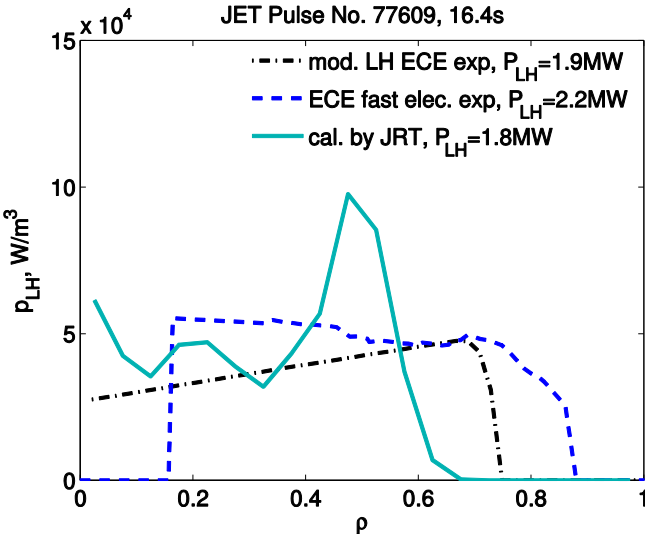

Figure 6: LH wave power deposition profiles of JET 3.4T/1.5MA low density pulse #77609. The JRT profile of p_{LH} (solid cyan line) was derived for a radial mesh of 21 points and with 2D fully relativistic, bounced-averaged FP and T_{e0}=1keV. The experimental profiles were determined from modulation experiments (dash-dotted black line) [43] and alternatively from the ECE of the supra-thermal electrons (dashed blue line) [44]. The total amount of experimentally assessed and calculated absorbed power, P_{LH}, in shown in the legends for all three cases.

The discrepancies between the experimental and theoretical power deposition profiles for $0.6<\rho<0.85$ is a typical feature of the so called spectral gap problem related to the modelling the LH waves absorption and CD [3], [7], [50]. Indeed, damping of LH waves

with $N_{||} \approx 2$ in this cold region, $T_e \approx 1$keV, would require either a significant fraction of supra-thermal electrons with $v > 10\ v_t$ or up-shift in $N_{||}$ spectrum. A number of plausible physical mechanisms have been proposed to explain the bridging of the spectral gap: wave scattering from density fluctuations [50], [51], wave diffraction, and parametric decay instabilities [52]. A spectral tail model as discussed in [50] with $N_{||}$ extended up to about 2.5 has been tested with JRT for the case shown in figure 6. The results of this test show broader power deposition profile with substantial LH wave absorption up to ρ≈0.7, which is more consistent with experimental observations.

JRT code was also tested at higher density JET 3.4T/1.8MA pulse #77612. As in the previous case the code provides more ragged power deposition profile, figure 7. Significant amount of power is predicted in the very core, while between ρ>0.1 and ρ<0.5 the code results in about twice higher power. As with the previous case, the deposition at the periphery is not matched: the code predicts no LH power for ρ>0.7, while there is experimental evidence that LH power is absorbed for up to ρ=0.8. The total absorbed power from JRT is 1.7MW, which is in a good agreement with the actual launched power of about 1.8MW. The total driven current has been assessed of order of $I_{LH} \approx 0.12MA$, figure 5b.

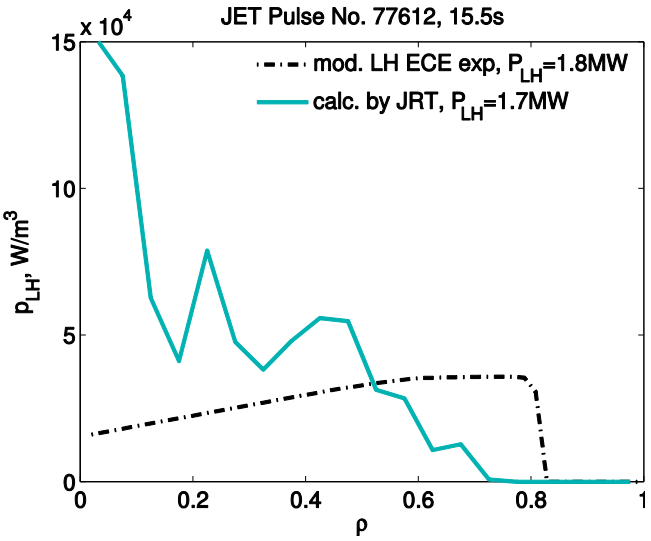

Figure 7: LH wave power deposition of JET pulse #77612 at 3.4T/1.8MA and $\bar{n}_e \approx 3 \times 10^{19}\ m^{-3}$, $T_{e0} \approx 3.5keV$. The JRT profile of p_{LH} (solid line) was derived for a radial mesh of 21 points and with fully relativistic, bounced averaged FP. The experimental profiles were determined from modulation experiments (dash-dotted line) only. The total driven current is assessed of order of 0.18MA.

From the two comparisons one can conclude that while the JRT code provides very consistent power deposition profiles as lower density, matching the experimental observations at higher density is more challenging. The good agreement observed at the lower density case indicates that the raytracing and FP codes are restricted to lower density cases only. The failure of the RT/FP codes at higher density is a well-known fact, [3].

Case study: LHCD during the preheat for JET AT scenario

Further to our studies the JRT code was successfully applied to study the LH power deposition and CD during the pre-heat phase of AT scenario 2.4T/1.5MA JET pulse #86814 [45], [46]. In this case ~1MW of LH power with spectrum peaked at $N_{||}$=1.83 was applied early in the current ramp-up phase in order to slow down the current penetration thus modifying the q-profile evolution. The results for five time-slices during the pre-heat simulations are shown in figures 8-10.

Time traces of pulse #86814 are shown in figure 8. LH power of about 1MW is applied at 1.5s after the breakdown up to 4.2s. The current and the density rise until about 2.5s. The electron temperature from the ECE, figure 8 bottom, shows typical fast electrons feature at the edge, R_A=3.8m, which intensity decreases with density increase.

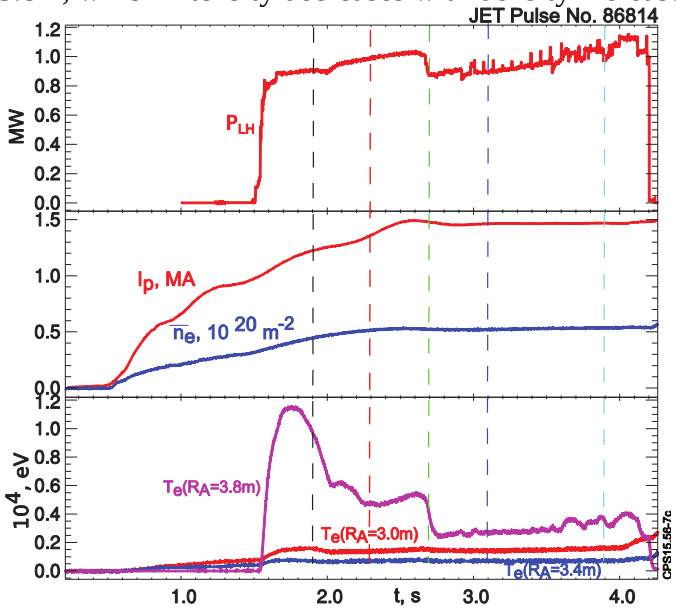

Figure 8: Time traces of AT scenario 2.4T/1.5MA JET pulse #86814 showing LHCD power at the top, plasma current, I_p, and line-integrated density, $\bar{n}_e$, middle graph and electron temperature, T_e, evolution in the core (R_A=3m), mid radius (R_A=3.4m) and at the edge (R_A=3.8m) at the bottom graph. Five time slices at which the profiles are taken and LH deposition and CD are studied are shown in black (1.9s), red (2.3s), green (2.7s), blue (3.1s) and cyan (3.9) vertical dashed lines.

The electron density and temperature profiles for the selected 5 colour coded time slices are shown in figure 9 a) and b). Electron density, figure 9 a), at the very first instant, 1.9s, is slightly hollow in the core, then it flattens at 2.3s and later it peaks with central values of about 3×10^{19}m^{-3}. Electron temperature, figure 9 b), almost does not change inside ρ<0.6. The EC emission due to the fast electrons' tails seen as a specific jump in the T_e profiles at the periphery and at the edge in all time slices have been neglected in the simulations as T_e profiles have been smoothed in this region.

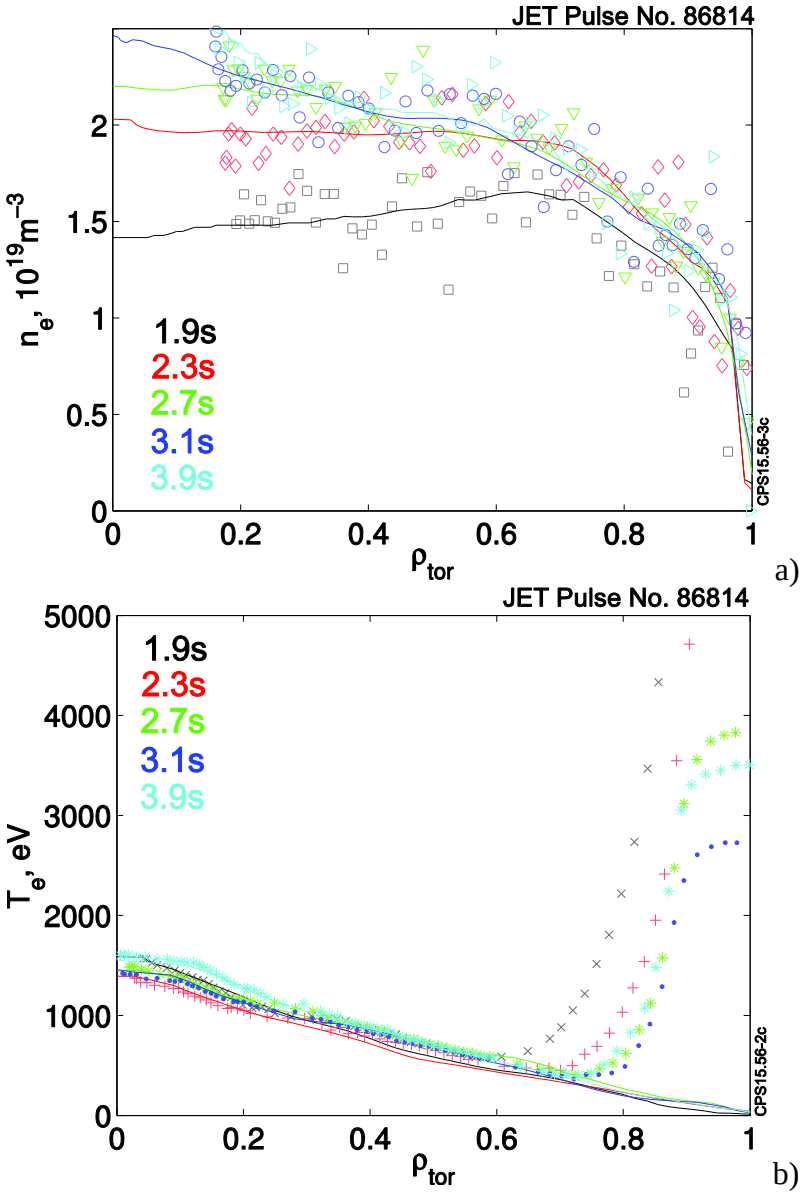

Figure 9: a) Electron density a), n_e, and temperature b), T_e, profiles and of five time slices shown in figure 8. The time instants are colour coded in the legend.

The power deposition and CD profiles calculated by JRT code with 2D relativistic bounce averaged FP are shown in figure 10 a) and b). Both the deposition and CD profiles are off-axis, relatively narrow and peaked at about ρ=0.55, in the first two instances, 1.9s and 2.3s, which correspond to slightly hollowed and flat density profiles. In the lowest density case the LH power is absorbed up to ρ≈0.73 and the code does not predict absorption at the cold plasma periphery, i.e. for ρ>0.8. The power deposition profiles have not been analysed experimentally in this case; however, it is unlikely large amount of microwave power to be absorbed at low temperature, T_e<250eV.

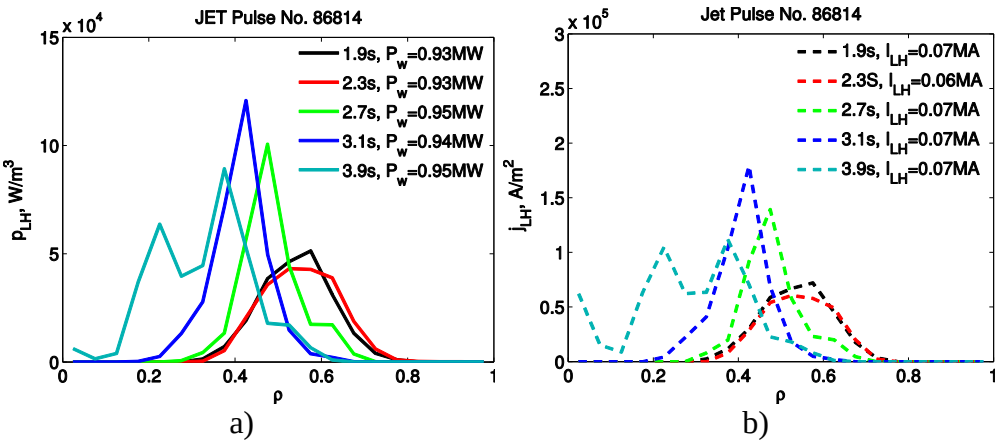

Figure 10: a) Power deposition profiles from the new code JRT with 3D relativistic FP with trapped particles results at the five time intervals; b) LH current drive for JRT. The total driven current at the five time slices is provided for comparison.

The power deposition and driven current peaks up and moves inward towards the core while density peaking increases from 2.7s to 3.9s, figure 10 a) and b). This observation is in quantitative agreement with observed supra-thermal emission from ECE as shown in figure 9 b). Indeed, by shifting the power deposition inwards the EC emission by the generated fast electrons becomes more effectively screened by the optically thick plasma. The coupled microwave power of about 1MW is absorbed almost 100% as the total amount of deposited power has been calculated between 0.93MW and 0.95MW.
The total driven current is 0.07MA and does not change throughout the simulation. The 1D FP code predicts CD of about 0.1MA, i.e. this approach overestimates the current by 50%.

CONCLUSIONS

A new RT/FP code was developed at JET to account for the complex plasma geometry and various $N_{||}$ spectra that can be launched from the antenna. RT code has been validated and coupled to three different FP solvers: 1D, 2D relativistic and 2D relativistic bounce averaged.
The solutions from the three codes were compared for a pair of low- and high-density plasmas and it was found that while the power depositions were consistent, the CD predicted by 1D code was about twice as high. The difference in power absorption and CD profile between 2D relativistic and 2D relativistic bounce averaged FP was negligible. The power deposition profiles were then compared to the experimentally assessed ones and it was concluded that in low density regime the RT/FP code reproduces well the experimental data. At high density the code predicts more on-axis deposition, while a broader profile has been observed from the ECE analysis.
The code was also used to study LH wave absorption and CD in SS scenario at JET where LHCD was applied during the low density pre-heat phase. It was found that LH deposition and CD are at the beginning off-axis and narrow and moves towards the core and broadens as density increases. A total current drive of about 70kA was calculated and it is lower than the results from 1D FP code.

Although the code was only discussed in terms of LH wave absorption and CD it can be also used to calculate the power deposition and CD by ECRH waves as well.

AKNOWLEDGEMENTS

This work has been carried out within the framework of the EUROfusion Consortium and has received funding from the Euratom research and training programme 2014-2018 under grant agreement No 633053. The views and opinions expressed herein do not necessarily reflect those of the European Commission.
Author K.K. gratefully thanks M. Shoucri for providing him with the magdi3 FP code and Bob Harvey from CompXCo for providing him with the latest versions of GENRAY and CQL3D codes.

REFERENCES

[1] Fish N, 1987, Rev. Mod. Phys. **59** 175
[2] Porkolab M, 1985, Wave Heating and Current Drive in Plasmas, eds. V Granatstein and P. Colestock, (Gordon and Breach Sci. Publishers, 1985), p.219
[3] Bonoli P, 2014, Phys. Plasmas **21** 061508
[4] Hoang G T *et al*, 2009, AIP Conf. Proc. Volume 1187, pp. 411-419, Radio Freq. Power in Plasmas, *18th Top. Conf. on Radio Freq. Power in Plasmas*
[5] Hoang G T *et al*, 2009, Nucl. Fusion **49** 075001
[6] Poli F *et al*, 2012, Nucl. Fusion **52** 063027
[7] Decker J *et al*, 2011, Nucl. Fusion **51** 073025
[8] Bonoli P, Proc. 21st Int. Conf. on Fusion Energy 2006 (Chengdu, China, 2006) (Vienna: IAEA) CD-ROM file IT/P1-2
[9] ITER Phys. Basis Expert Group, 1999, Nucl. Fusion **39** 2495
[10] Gormezano G *et al*, 2007, Nucl. Fusion **47** S285
[11] Kessel C E *et al*, 2007, Nucl. Fusion **47** 1247
[12] Bernstein I, 1975, Phys. Fluids **18** 320
[13] Brambilla M, Cardinali A, 1982, Plasma Physics **24** 1187
[14] Pereverzev G, 1992, Nucl. Fusion **32** 1091
[15] Bertelli N *et al*, 2012, Phys. Plasmas **19** 082510
[16] Wright I *et al*, 2009, Phys. Plasmas **16** 072502
[17] Shiraiwa S *et al*, 2010, Phys. Plasmas **17** 056119
[18] Cardinali A, Zonca D, 2003, Phys. Plasmas **10** 4199
[19] Lu Z *et al*, 2013, Phys. Plasmas **20** 032115
[20] Bao J *et al*, 2014, Plasma Phys. Control. Fusion **56** 095020
[21] Kennel C, Engelmann F, 1966, Phys. Fluids **9** 2377
[22] Kupfer K, Moreau D, 1992, Nucl. Fusion **32** 1845
[23] Kupfer K *et al*, 1993, Phys. Fluids B **5** 4391
[24] Esterkin A, Piliya A, 1996, Nucl. Fusion **36** 1501
[25] Baranov Yu *et al*, 1996, Nucl. Fusion **36** 1031
[26] Barbato E *et al*, 2014, Nucl. Fusion **54**
[27] Bonoli P, 1984, IEEE Trans. Plasms Phys. p.195
[28] Bonoli P, Englade R, 1986, Phys. Fluids **29** 2937

[29] Ignat D *et al*, 1994, Nucl. Fusion **34** 837
[30] Smirnov, Harvey B, 1995, Bul.Am.Phys.Soc **40**1837
[31] Peysson Y *et al*, 2012, Plasma Phys. Control. Fusion **54** 045003
[32] Imbeaux F, Peysson Y, 2005, Plasma Phys. Control. Fusion **47** 2041
[33] Ding B *et al*, 2011, Phys. Plasmas **18** 082510
[34] Karney C, 1986, Comput. Phys. Rep. **4** 182
[35] Shoucri M, Shkarofsky I, 1994, Comp. Phys. Comun. **82** 287
[36] Peysson Y, Shoucri M, Shkarofsky I, 1998, Comp. Phys. Comun. **109** 55
[37] Simonetto A *et al*, 2000, "A numerical code for solution of the relativistic bounce-averaged FP equation", IFP Internal report FP 00/08
[38] Kerbel G, McCoy M, 1985, Phys. Fluids **28** 3629
[39] Killeen J, Kerbel G, McCoy M, Mirin A, 1985, Computational methods for kinetic models of magnetically confined plasmas, Springer-Verlag
[40] Harvey R, McCoy M, The CQL3D Fokker-Planck Code, 1992, General Atomics Report GA-A20978
[41] Litaudon X, Moreau D, 1990, Nucl. Fusion **30** 471
[42] Brambilla M, 1979, Nucl. Fusion **19** 1343
[43] Kirov K *et al* 2010, Nucl. Fusion **50** 075003
[44] Kirov K *et al* 2012, Plasma Phys. Control. Fusion **54** 074003
[45] Joffrin E *et al* 2014'Advanced scenario development with the JET ITER-like wall' ITPA-IOS conference
[46] Joffrin E *et al* 2014 'JET contribution to the research on steady state operation' 8th IAEA Technical Meeting on Steady State Operations of Magnetic Fusion Devices
[47] Bizarro J and Moreau D, 1993, Phys. Fluids B **5** 1227
[48] Bizarro J, 1993, Nucl. Fusion **33** 831
[49] Peysson Y and Decker J, 2014, Fusion Sci. and Technology **65** 22
[50] Decker J *et al* 2013, AIP Conf. Proc. Volume 1580, pp. 129-136, Radio Freq. Power in Plasmas, *20th Top. Conf. on Radio Freq. Power in Plasmas*
[51] Peysson Y *et al* 2011 Plasma Phys. Control. Fusion **53** 124028
[52] Cesario R *et al* 2010 Nature Commun. **1:55**, 1-10